Structural Monitoring and Maintenance, *Vol. 9, No. 4 (2022) 373-388*
https://doi.org/10.12989/smm.2022.9.4.373

Depth estimation for surface-breaking cracks in steel-fiber reinforced concrete using ultrasonic surface waves

Ahmet S. Kirlangic*[1] and Zafer Iscan[2]

[1]*Department of Engineering, Teesside University, Middlesbrough, United Kingdom*
[2]*Department of Electrical and Electronical Engineering, Faculty of Engineering and Natural Sciences, Bahcesehir University, Istanbul, Turkey*

(*Received October 25, 2022, Revised November 24, 2022, Accepted December 8, 2022*)

Abstract. A USW based diagnostic procedure is presented for estimating the depth of surface-breaking cracks. The diagnosis is demonstrated on seven lab-scale SFRC beam specimens, which are subjected to the CMOD controlled three-point bending test to create real bending cracks. Then, the recorded multiple ultrasonic signals are examined with the signal processing techniques, including wavelet transform and two-dimensional Fourier transform, to investigate the relationships between the crack depth and two diagnostic indices, namely the attenuation coefficient and dispersion index (DI). Finally, the reliabilities of these indices for depth estimation are verified with the visually measured crack depths as well as the crack features obtained with a digital image processing algorithm. It is found that the DI outperforms the attenuation coefficient in depth estimation, where this index displays good agreement with the visual inspection for 86% of the inspected specimens.

Keywords: attenuation; condition assessment; crack depth estimation; dispersion; fiber-steel reinforced concrete; NDT for concrete; surface-breaking cracks; ultrasonic surface waves

1. Introduction

Non-destructive tests (NDT) are becoming widely used for the condition assessment of concrete structures. Currently, there exists a diverse range of commercial NDT devices developed for a variety of applications. The techniques particularly based on ultrasound, acoustic emission (AE), ground penetrating radar (GPR), and electrical resistivity (ER) have found widespread use in the industry. Among these techniques, the ultrasonic methods examine the mechanical waves in ultrasonic range propagating in concrete (ASTM C597-16, ASTM C1383-15), whereas the AE is designed to track the energy release occurring during cracking (Carpinteri *et al*. 2011). The GPR, on the other hand, is based on monitoring the propagation of electromagnetic waves. Although the GPR is actually a geophysical application developed to picture the subsurface soil profiles, it can also be used to determine thickness of concrete pavements and locate the reinforcement (Daniels 2004). Lastly, the ER measures the response voltage in concrete due to an applied electrical current, and is used to detect corrosion of rebars in the reinforced concrete (ACI-222R-01 2010). In addition to these well-established NDT techniques for the assessment of concrete structures, the recent research

*Corresponding author, Ph.D., E-mail: s.kirlangic@tees.ac.uk

Copyright © 2022 Techno-Press, Ltd.
 ISSN: 2288-6605 (Print), 2288-6613 (Online)

efforts mostly focus on the applications of digital image processing techniques; in the imaged based assessment, the cracks/defects visible on the concrete surface are aimed to be detected and classified in an automated manner (Tang and Chen 2020, Dorafshan *et al*. 2018). Nevertheless, all of the above techniques still lack accurate depth estimation for surface-breaking cracks, which is the foremost concern to determine the remaining capacity of any structural member.

The accurate depth estimation for the surface-breaking cracks, which is the main goal of this study, can be realized with the adaptation of the current ultrasonic methods. The most common ultrasonic tests for the condition assessment of concrete are the ultrasonic pulse velocity (UPV) and impact echo (IE); both base on observing the P-waves (ASTM C597-16, ASTM C1383-15). While the former is primarily used to assess the material's elastic modulus, the latter is preferred to measure the material thickness and detect the embedded defects. By adapting the transducer configuration in these methods, it is possible to evaluate the depth of the surface-breaking cracks by measuring the travel time between the source and receiver transducers; however, the depth estimation based on the time-of-flight principle may result in misleading results depending on the shape and orientation of the crack tip (Song *et al*. 2003). This shortcoming of the conventional ultrasonic tests can be overcome by examining the ultrasonic surface waves (USW). The USW are already used for non-destructive testing in a range of applications; such as detection of underground infrastructure (Tallavo *et al*. 2009), surveying for underground cavities (Nasseri-Moghaddam *et al*. 2007), quality assurance for pavements (du Tertre *et al*. 2020), assessment of bonding quality between fiber-reinforced-plastic and concrete (La Malfa Ribolla *et al*. 2018), and condition assessment of concrete members (Kee *et al*. 2015, Kirlangic *et al.* 2016, Kirlangic *et al*. 2020, Rodríguez-Roblero *et al*. 2019). The USW based methods enable to monitor the wave attenuation and dispersion; because these wave characteristics are altered in the presence of any crack, even in the case of those with touching faces, they can be used to evaluate the crack depth as well.

Surface waves attenuate as they propagate in accordance with the material properties. If these propagating surface waves are recorded at different source offsets, the material attenuation coefficient can be determined by measuring the change in the wavelength amplitudes. Since the attenuation coefficient is a characteristic feature of the material, it is possible to detect and quantify the size of defects in the material. A second diagnostic feature that can be extracted from the USW is the dispersion in phase velocities of surface waves. In unbounded solid bodies, all wavelengths move at the same velocity; whereas, in the case of an obstacle, such as a crack or void, those wavelengths that are proportional to the dimensions of the obstacle exhibit dispersive behavior. In other words, the velocities of such wavelengths change compared to those wavelengths that do not interact with the obstacle. This situation is known as wave dispersion and can be used for damage assessment.

Surface breaking cracks occur mostly under bending and align in vertical direction with respect to the load. Evaluation of the depth of such cracks by the means of ultrasonic methods are previously targeted by many researchers. In the previous studies, however, the cracks are modelled as artificial clear-cut notches in laboratory specimens and numerical models, rather than being represented with the complex shaped real bending cracks (Zerver *et al*. 2003, Yang *et al*. 2009, Kirlangic *et al*. 2015). These studies conducted on the artificial cracks reveal satisfactory results in depth estimation using the frequency dependent surface wave features. Nevertheless, the extraction and interpretation of the wave features obtained from the signals recorded on the real structural concrete elements require improvement of the test configuration and utilization of advanced signal processing techniques. Therefore, there is a need for a detailed investigation on the real bending cracks in order to determine their depth, and hence their remaining cross-sectional area.

To fulfil this gap, herein an experimental campaign is pursued on steel-fiber reinforced concrete (SFRC) beam specimens comprising realistically created bending cracks of different depths. In order to develop the diagnostic procedure that evaluates the depth of surface breaking cracks, a multi-channel test configuration is implemented on these SFRC beams. The recorded USW signals are examined to understand the relationships between the crack depth and the diagnostic features, namely the attenuation coefficient and dispersion index (DI). The attenuation coefficient is determined by utilizing wavelet transform while the dispersion index is extracted using two-dimensional Fourier transform. These diagnostic features measured for depth estimation are finally verified with the visually measured crack depths as well as the crack features obtained with a digital image processing (DIP) algorithm developed for this study. The SFRC beam specimens are preferred in this study for two reasons: (i) first, the crack mouth opening displacement (CMOD) controlled bending test to create certain depths of bending cracks can be conveniently performed on them, unlike relatively large reinforced concrete beams; and (ii) secondly, although the non-destructive testing for the SFRC were investigated to some extent previously using the conventional ultrasonic methods, these research activities focused on material characterization for the SFRC rather than crack depth estimation (Yazici *et al*. 2007, Acebes *et al*. 2011, Van Hauwaert *et al*. 2020, Katzer *et al*. 2020). The only notable study targeting to assess the crack depth in SFRC is performed by monitoring the Rayleigh wave velocity (Aggelis *et al*. 2012), where it is found that the wave amplitude is more sensitive to the crack depth compared to the wave velocity. Therefore, herein the wave characteristics other than wave velocity, namely attenuation and dispersion, are investigated for the crack depth estimation in the SFRC.

.

2. Background on mechanical wave characteristics

2.1 Attenuation

Attenuation in propagating waves occurs due to geometric radiation and material damping. The spatial attenuation coefficient α_x, which is associated with the material damping, is determined from a propagating wave by (Richart *et al*. 1970)

$$\alpha_x = \frac{1}{x_{i+1} - x_i}\left[ln\left(\frac{A_{i+1}}{A_i}\right) - \beta\, ln\left(\frac{x_{i+1}}{x_i}\right)\right] \tag{1}$$

where A_i is a wave quantity at distance x_i with respect to the excitation source, and β is the geometric attenuation constant, which is equal to -0.5 for the surface waves due to their cylindrical wave front. The wave quantity A_i can simply be the amplitude in time signal, or any magnitude associated with a specific frequency extracted using signal processing techniques, such as the Fourier or wavelet transforms. The wavelet transform is superior to the conventional Fourier transform since temporal information is kept after the transformation. The continuous wavelet transform (CWT) of a signal $p(t)$ is given as (Addison 2002)

$$WT(a,b) = \frac{1}{\sqrt{a}}\int_{-\infty}^{\infty} p(t)\psi^*\left(\frac{t-b}{a}\right)dt \tag{2}$$

where $\psi(t)$ is called the mother wavelet function, a is the dilation parameter and b is the location parameter for time shift. The dilated and shifted wavelet function is denoted as

$\psi(t-b/a)$, and ψ^* is its complex conjugate. Eq. (2) enables to examine any frequency by substituting an appropriate dilation parameter a. However, if a broader frequency range is targeted, then, instead of the CWT, the discrete wavelet transform (DWT) will be more efficient. By utilizing the DWT, any signal $p(t)$ can be decomposed into its sub-signals, of each is associated with a specific frequency bandwidth, which requires the following discretized mother wavelet (Addison 2002)

$$\psi_{j,k}(t) = \frac{1}{\sqrt{a_0^j}}\psi\left(\frac{t-k\tau_0 a_0^j}{a_0^j}\right) \tag{3}$$

where j and k are integers, the fixed dilation step $a_0 = 2$, and the translation factor $\tau_0 = 1$. In this study, the DWT is preferred to determine the attenuation as it is demonstrated by Kirlangic *et al.* (2016) as a reliable and convenient method.

Herein, the attenuation coefficient will be calculated by processing the ultrasonic signals acquired at different distances with respect to a source transmitter on a specimen including a certain depth of crack. As illustrated in Fig. 1, in the first step of the proposed data processing routine, the raw signals will be initially subjected to the DWT in order to decompose the recorded signals into their sub-signals of different frequency bandwidths, so that the most prominent frequencies in the signals can be examined. In the second step, the selected sub-signals will be processed with the conventional Fourier transform to obtain their spectral densities. Then, the cumulative spectral energy of these selected sub-signals will be subjected to regression analysis with respect to the source offset to determine the attenuation coefficient. Finally, all these steps will be repeated for a variety of specimens with various crack depths, so that the correlation of the attenuation coefficient with the crack depth can be clearly demonstrated for the purpose of damage diagnosis.

2.2 Dispersion

Surface waves propagate near the surface boundary of a medium by the combined acts of both horizontal and vertical particle displacements, and carry two thirds of the wave energy (Graff 1975). In homogeneous half space, the surface waves propagate at a constant Rayleigh wave velocity V_R. However, in the case of a geometrical boundary, such as a defect or crack, the surface waves may exhibit dispersive behavior since the wave reflections and refractions caused by the crack will interact with the initial wave propagation. Dispersion can be described as the variation in the velocity of different frequencies travelling through a medium; in other words, the frequency-dependent wave velocity, which is known as the phase velocity. The wavelength λ is related to the phase velocity V_{ph} and frequency f by

$$\lambda = V_{ph}/f \tag{4}$$

The dispersion in propagating waves can be visualized with a plot of phase velocity vs. frequency, which is called the dispersion curve. The procedure for the detection of dispersion in the surface waves can be summarized in three steps: (i) acquisition of the time signals (time-offset domain), (ii) transformation of the data from the time-offset domain $(x-t)$ into a frequency-wavenumber domain $(f-k)$, and (iii) extraction of the phase velocity (dispersion curve). The $f-k$ plot represents the relationship between wavenumber k and frequency f; whereas the wavenumber is related to the wavelength by

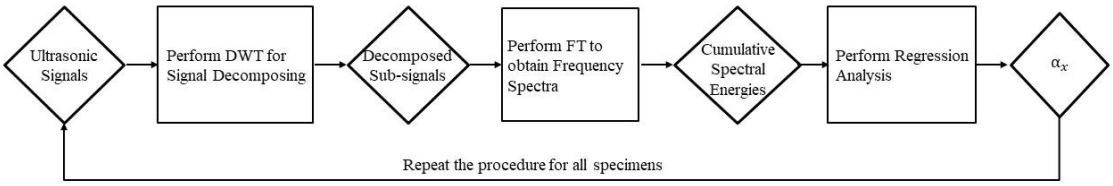

Fig. 1 Flow-chart to determine the attenuation coefficient

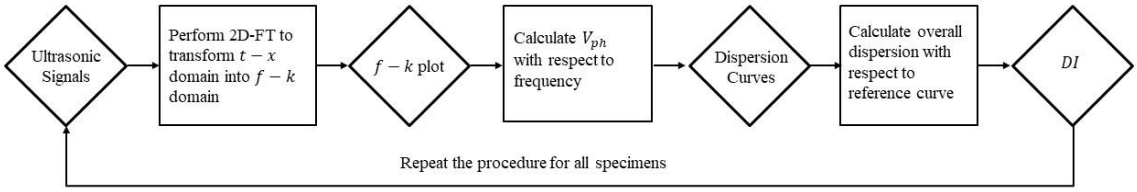

Fig. 2 Flow-chart to determine the dispersion index

$$k = 2\pi/\lambda \tag{5}$$

And from Eqs. (4) and (5)

$$V_{ph} = 2\pi(f/k) \tag{6}$$

Eq. (6) provides the phase velocities V_{ph} to be determined from the $f-k$ plot, which are then used to constitute the dispersion curve. Once the dispersion curve is obtained, it can be used as a diagnostic tool to estimate the condition of the inspected medium.

The dispersion in wave propagation can be determined experimentally by utilizing a multi-channel test configuration, which allows acquiring multiple time signals at different locations. Then, the two-dimensional Fourier transform (2D-FT) of the captured signals is performed to obtain a two-dimensional spectrum in frequency-wavenumber domain ($f-k$ plot), where the incident, reflected and transmitted waves can be identified. The peaks in the plot are used to compute the phase velocities which constitute the dispersion curve of each event. In the case of a homogeneous half-space medium, the dispersion curve appears as a straight line with a slope equal to the V_R. However, any disruption in the phase velocity due to any anomaly appears in the $f-k$ plot, which can be used to interpret the damage condition. In this work, the dispersion curves attained from experiments are used to define a diagnostic parameter called "dispersion index" (*DI*), which relates the dispersion in phase velocity V_{ph} to the damage content as (Kirlangic *et al*. 2016)

$$DI^{\langle Damaged\rangle} = \sum \frac{\left|V_{ph}^{\langle Damaged\rangle}(f) - V_{ph}^{\langle Intact\rangle}(f)\right|}{V_{ph}^{\langle Intact\rangle}(f)} \tag{7}$$

The dispersion index is basically the cumulative variation in phase velocity caused by the crack normalized with respect to the reference dispersion curve representing the intact case. This reference dispersion curve can be obtained by the Rayleigh-Lamb frequency equation defined as (Graff 1975)

$$\frac{\tanh(\beta d)}{\tanh(\alpha d)} + \left[\frac{4\alpha\beta k^2}{(k^2-\beta^2)^2}\right]^{\pm 1} = 0 \qquad \begin{cases} +1 = symmetrical \\ -1 = antisymmetrical \end{cases} \tag{8}$$

where $\alpha^2 = \kappa^2 - \omega^2/V_p^2$ and $\beta^2 = \kappa^2 - \omega^2/V_s^2$. V_P and V_S are the P-wave (Primary wave) and S-wave (Shear wave) velocities; whereas κ, ω and d are the wavenumber, angular frequency and medium thickness, respectively. The first antisymmetrical Lamb mode obtained from Eq. (8) can be employed as the reference dispersion curve to calculate the *DI* given in Eq. (7). The S-wave velocity V_S, which is required in Eq. (8) is calculated based on the Rayleigh wave velocity V_R and the Poisson ratio ν by (Graff 1975)

$$V_S = \frac{1+\nu}{0.87+1.12\nu} V_R \tag{9}$$

The data processing procedure proposed above to determine the *DI* is summarized in Fig. 2.

3. Experimental methods

3.1 Beam specimens

Seven laboratory scale steel-fiber reinforced concrete (SFRC) beams (50x10x10 cm3), of which concrete mix consists of 1,054 kg coarse aggregate, 797 kg sand, 310 kg CEM I 42.5R type cement, 202 kg water, 3.5 kg superplasticizer, and 39.3 kg 35-mm-long hook-end steel-fiber, are produced. Following 28-day curing period, six of the beams are subjected to three-point bending test in accordance with EN 14651 (2005) in order to create real-shaped cracks due to bending. During the bending tests, the crack mouth opening displacement (CMOD) is monitored, and once a predetermined crack width is reached, loading is aborted; so that a different crack depth for each beam could be reached. The loading paths and the cracks created in each beam are shown in Figs. 3-4, respectively. The beams are named after B0, B1, B2, B3, B4, B5, and B6; as the increasing number refers to increasing CMOD; which varies from 1.00 mm to 2.25 mm with an increment of 0.25 mm. B0 is not subjected to bending test in order to reserve it as the control beam. The crack depths measured visually are found ranging from 53 to 94 mm as given in Table 1. The bending strength, on the other hand, is determined ranging between 3.65 MPa and 5.34 MPa (Table 1), of which average strength is 4.64 MPa. Finally, the compressive strength is measured as 31.8 MPa from three standard size cylindrical specimens tested in comply with EN 12390.

3.2 Digital image processing

In addition to the crack depths measured with the visual inspection, a digital image processing (DIP) algorithm is developed in MATLAB environment to quantify the crack depths and areas on the images of cracks. The developed DIP algorithm consists of the following steps:

- Image cropping: To shorten the processing time, images are cropped as to keep only the cracked area and the R channel of the RGB image was selected to be processed in the following steps.
- Filtering (smoothing): Filtering is performed to remove noise using a blurring function.

- Edge detection: The shapes of cracks are revealed by edge detection with Canny edge detectors. This operation generates a binary (black and white) image.
- Morphological operation: The crack shapes obtained by edge detection are dilated and small objects corresponding to noise in the binary images are removed. The gaps in the cracks are filled using morphological closing.
- Crack merging: Individual crack shapes positioned close to each other are connected.
- Crack size calculation: The crack length and area are calculated over the combined crack form

The photograph of each beam is processed with the DIP algorithm, and the crack forms shown in Fig. 5 are obtained. The crack lengths and areas given in Table 1 are calculated by using the crack

Table 1 The beam properties

Beam	Bending Strength (MPa)	CMOD (mm)	Crack Depth[1] (mm)	Crack Depth[2] (mm)	Crack Area[2] (mm^2)
B0	N/A	N/A	N/A	N/A	N/A
B1	5.34	1.00	53	51.5	50.95
B2	4.79	1.25	5 8	61.5	60.61
B3	3.65	1.50	79	79.6	68.19
B4	4.49	1.75	76	75.0	43.23
B5	4.63	2.00	90	64.9	73.26
B6	4.93	2.25	94	73.1	91.66

[1]Based on visual inspection, [2]Based on image processing

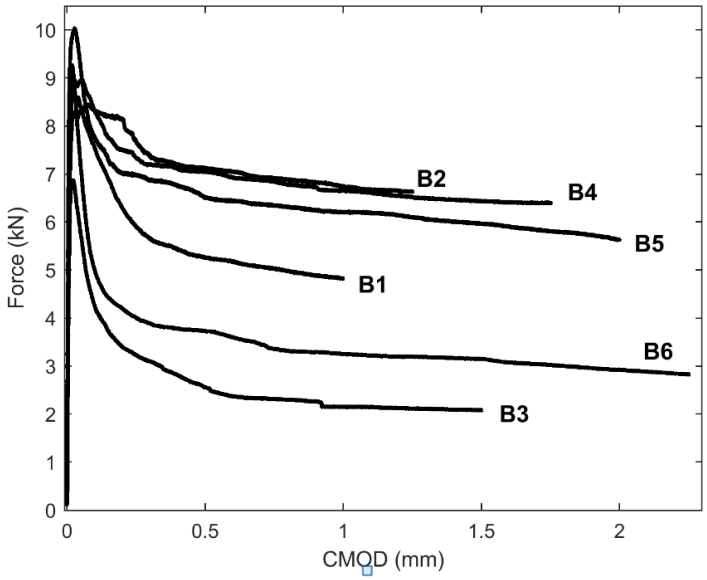

Fig. 3 The load vs. crack width curves from the bending tests

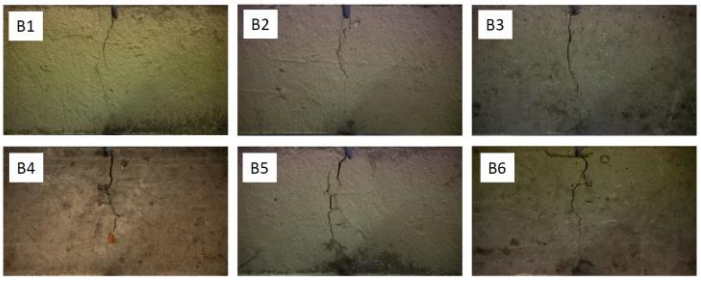

Fig. 4 The beams with cracks

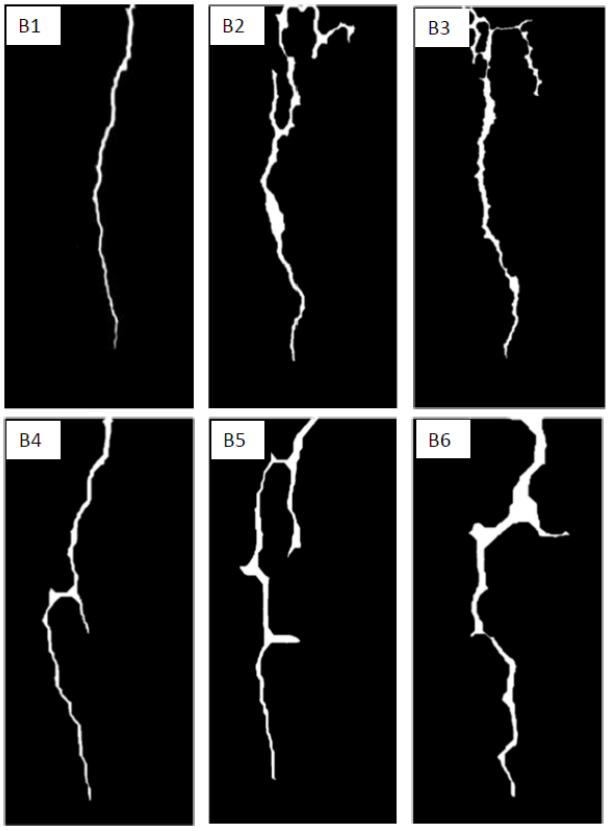

Fig. 5 Images of cracks obtained by the image processing algorithm (Images are not scaled)

forms appearing on these processed images. As given in the table, the crack depths obtained with the DIP are in agreement with the visually measured crack depths, except for two beams (B5 and B6). In addition to the crack depth, the crack surface area is calculated as a complementary damage measure with the DIP algorithm. B5 and B6, whose crack depths could not be determined correctly, are found to be the two most damaged beams based on the crack area.

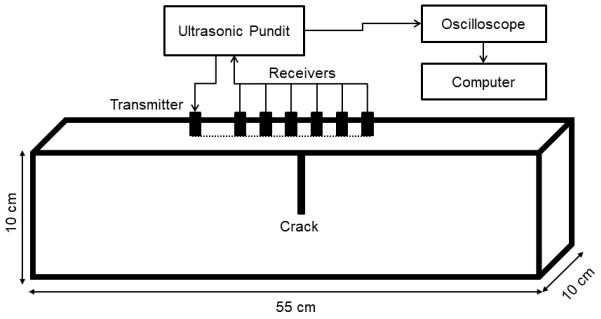

Fig. 6 Ultrasonic test configuration

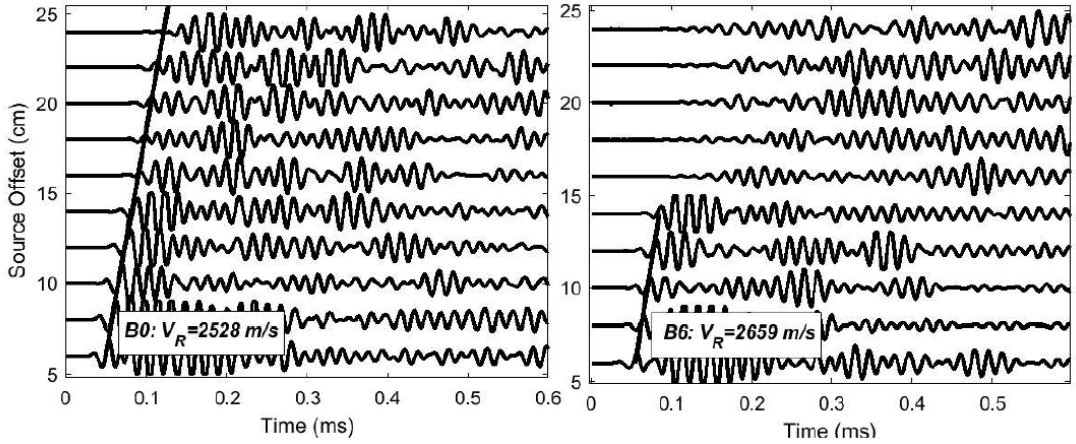

Fig. 7 Time history for each receiver for (left) B0 and (right) B6

3.3 Ultrasonic tests

The ultrasonic test instrumentation consists of an ultrasonic pundit (Proceq Pundit Lab), two transducers with 54 kHz resonant frequency, a two-channel oscilloscope, and a computer. One of the transducers is mounted 15 cm away from the crack to be used as the transmitter, whereas the other one, which is deployed as the receiver, is shifted along an 18-cm-long array. The receiving transducer is moved to ten different locations, of each separated 2 cm apart as illustrated in Fig. 6. The transmitter has 6 cm source offset with respect to the first location of the receiver. The coupling between the transducers and the beams are achieved by vacuum grease. At each location, one signal is recorded after averaging the acquired 100 signals. At the end of the ultrasonic tests, for each beam, a data set consists of 10 signals are attained.

4. Results and discussions

The time histories recorded on the intact beam (B0) and the one with the deepest crack (B6) are normalized and plotted in Fig. 7. A significant reduction in the wave-front of the surface waves after

the crack can be clearly observed in the time histories obtained from B6. For this beam, the maximum amplitude in the receiver #6 (R6) is measured approximately equal to only 10% of its neighbor receiver #5 (R5), which accounts for 90% drop in the wave energy. The R-wave velocity V_R shown on the time histories in Fig. 7, which is calculated based on the arrival times, is found as 2528 m/s for the intact beam. On the other hand, for B6, due to the crack, two different patterns of surface wave velocity, one before and the other after the crack, are detected. Before the crack, the V_R is determined 2659 m/s, which is in good agreement with the measured velocity on B0, while after the crack no clear arrival time is detected. The crack damps the initial wave-front significantly, resulting in a weak one followed by stronger refracted waves from the crack tip. Since the wave front passing the crack becomes so weak, the V_R could not be determined with high confidence, and thus is not considered as a measure of the crack depth.

4.1 Attenuation

The filtering effect of the cracks on the wave energy in the beam specimens can be clearly observed on the spectral energy plots given for beams B0, B2, and B6 in Fig. 8. For B0, which is the intact specimen, all frequencies seem to propagate along the beam. Whereas, in B2, which inherits a 58-mm-depth crack, the damping effect of the crack on the spectral energy is obvious. The crack causes a substantial damping on all frequencies; yet lower frequencies, in other word larger wavelengths, seem to survive the crack to some extent. Lastly, regarding B6, whose crack depth (94 mm) is almost equal to the beam cross-section (100 mm), no frequency could manage to pass through the crack as expected. This apparent damping effect of cracks on frequencies observed in Fig. 8 can be quantified with the attenuation coefficient given in Eq. (1). If Eq. (1) is adapted as to take into account only the energy of selected frequencies, rather than the entire spectral energy, it can be possible to determine the crack depth by examining the damping levels of the different frequencies. For this purpose, herein, instead of Fourier transform, the recorded signals are processed with the discrete wavelet transform (DWT) to determine the wave attenuation. The raw signals are first decomposed into sub-signals by deploying the Daubechies (dbn18) function defined in MATLAB as the main wavelet in the DWT. The decomposition of the raw signals with the DWT results in multiple decomposed sub-signals, of each is called a “level”. Each of these levels is associated with a specific frequency bandwidth, and hence a certain range of wavelengths. As an example, the attenuation curves for the spectral energies of these sub-signal levels obtained from the recorded signals along the receiver array on B0 are shown in Fig. 9. Each curve represents the attenuation for a specific frequency bandwidth in the figure; where it is apparent that the attenuation is faster in high frequency ranges, while it is less in low frequencies.

In this study, among different levels, the one representing the frequency bandwidth of 31-62.5 kHz, which overlaps with the transmitter’s bandwidth, is chosen and subjected to the Fourier transform to calculate the spectral energy at each receiver location to determine the attenuation. The attenuation trends shown in Fig. 10(left) present a decrease in the spectral energy of these sub-signals for B0 and B6. Since the beams have equal dimensions, the contribution of geometrical attenuation to the total attenuation is not eliminated as it is same for all beams. Therefore, the crack depth is evaluated based on the total attenuation α by fitting the attenuation trends to $e^{\alpha(x_1-x_i)}$, where x_i is the distance to the source transducer. The computed coefficient α for each beam is normalized and displayed in Fig. 10(right), where a significant increase in attenuation, almost 18 times, is apparent between the intact and the most damaged beams. Fig. 10(right) suggests that the crack depth in B1, B2 and B4; and B3, B5, and B6 should be close to each other. Since the sub-signal level

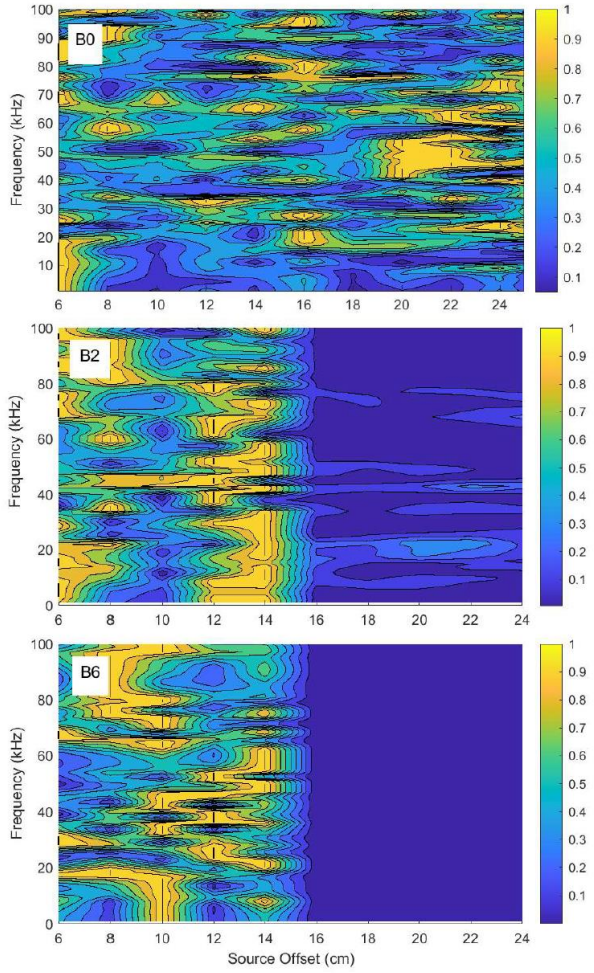

Fig. 8 Spectral energy along the receiver array (top) B0, (middle) B2, (bottom) B6

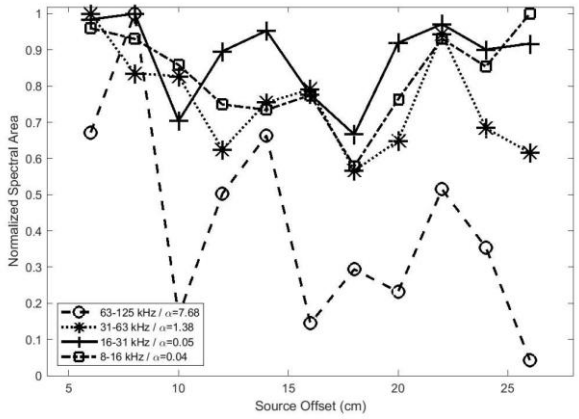

Fig. 9 Spectral energy per decomposed sub-signals obtained from B0

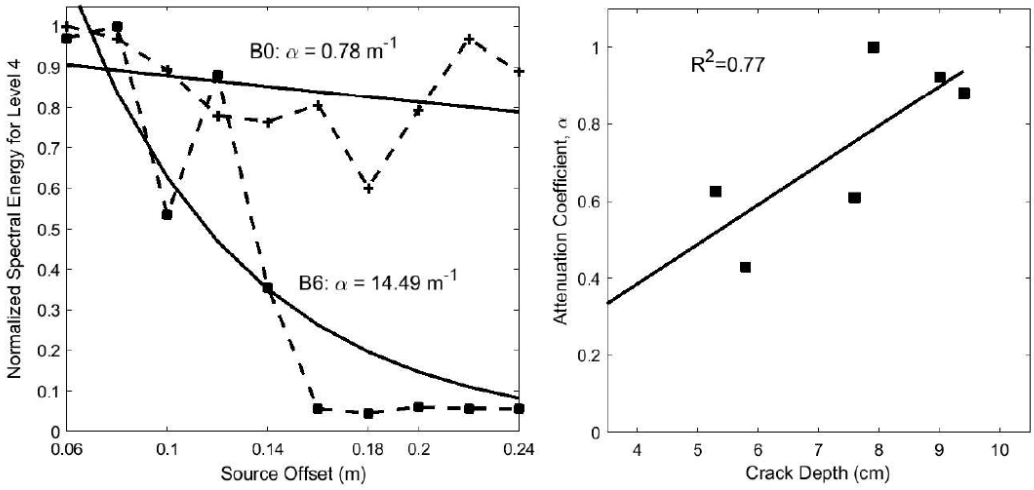

Fig. 10 (left) Attenuation trends, (right) Attenuation coefficient of the beams

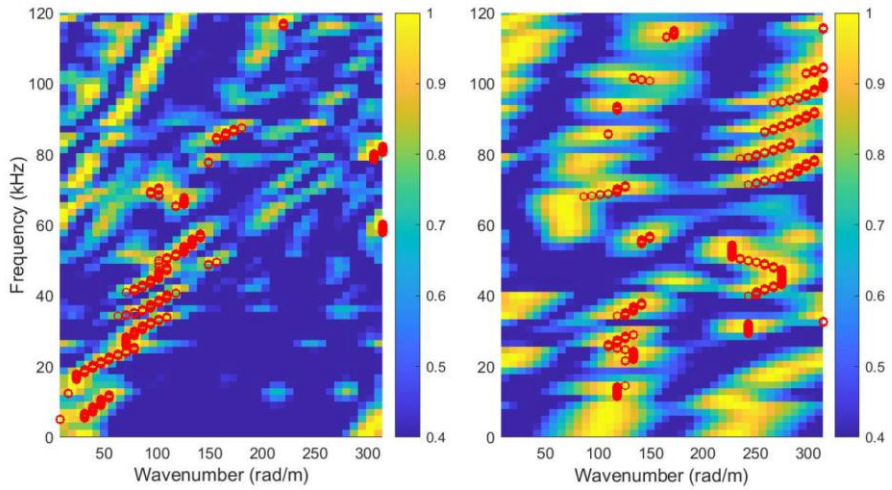

Fig. 11 The frequency-wavenumber ($f - k$) plot for (left) B0, (right) B6

is corresponding to the wavelengths between 4 and 8 cm, it can be predicted that the crack depth is at least 8 cm in B3, B5, and B6, which is all in agreement with the measured depth given in Table 1 for these three beams. The variation in attenuation displayed in Fig. 10(right) is in good agreement with the visually measured depth of the superficial cracks given in Table 1 for B1, B2, B5, and B6; whereas B3 and B4 exhibit contradictory results indicating that the depth of surface cracks observed on these two beams may vary throughout the beam cross-section.

4.2 Dispersion in phase velocity

In order to obtain the dispersion curves of the phase velocity V_{ph}, initially two-dimensional Fourier transform (2D-FT) is performed on the recorded signal array for each beam, so that the

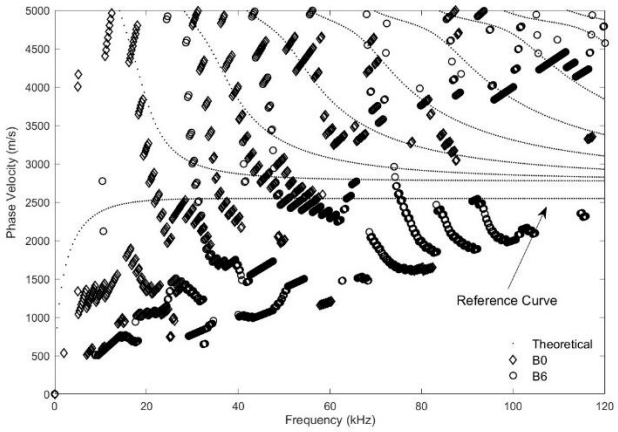

Fig. 12 The dispersion curves

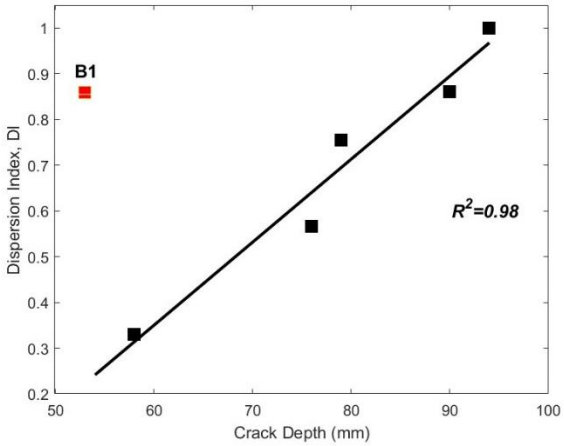

Fig. 13 The DI vs. Crack depth

frequency-wavenumber plots, as shown in Fig. 11, can be generated. Once, the $f-k$ plots are derived, the phase velocity is obtained for each frequency by selecting the associated wavenumber pointed by the maximum peak as indicated in the $f-k$ plots given for B0 (left) and B6 (right) in Fig. 11. The dispersive effect of the crack on the phase velocity is clearly observable on the $f-k$ plot for B6 with respect to the intact beam B0. Yet, the quantification of the dispersion in velocity requires further data manipulation. For this reason, the V_{ph} is computed using Eq. (6), and then is plotted (the dispersion curves) as shown in Fig. 12. The calculation of the overall dispersion, as described in Eq. (7), requires a reference dispersion curve that represents the first anti-symmetrical (flexural) Lamb mode, which is displayed along with the experimental dispersion curves in Fig. 12. This theoretical flexural mode is derived using the Rayleigh-Lamb frequency equation (Eq. (8)) for a 10-cm-thick concrete plate of which has a P-wave velocity of 4513 m/s and V_R = 2528 m/s, in accordance with the intact beam B0, and the Poisson's ratio $\nu =$ 0.2. The disruption in the dispersion curves pictured in Fig. 12 is then quantified with the dispersion index DI as defined in Eq. (7). The control specimen B0 is found to display the smallest index, DI = 0.165, as expected;

Table 2 Summary of the Results

Beam	Crack Depth[1] (mm)	α[2]	DI[3]
B0	N/A	0.047	0.165
B1	53	0.626	0.860
B2	58	0.429	0.330
B3	79	1	0.755
B4	76	0.610	0.566
B5	90	0.923	0.861
B6	94	0.882	1

[1]Based on visual inspection, [2]Normalized attenuation coefficient, [3]Dispersion Index

since no crack exists in this beam, the dispersion is solely caused due to the beam geometry. For the rest of the beams, the normalized DI is presented against the measured crack depth in Fig. 13. In this figure, the DI is observed to increase in general with the crack depth, except for B1, which presents an unexpected outlier value. The cause of this abnormally large dispersion in B1 could not be clarified; however, it is most likely that the relatively shallow crack depth visible on the beam surface is not representing the inner formation of the crack. According to the plot in Fig. 13, DI, which is the indicator of total dispersion in beams, increases in proportion to the crack depth, as observed in the attenuation coefficient earlier. The coefficient of determination $R^2 = 0.98$ as a result of the linear regression analysis performed for the five samples given in Fig. 13, where the undamaged specimen B0 and B1 with outlier value are not included.

5. Conclusions

In this paper, the depths of bending cracks in steel-fiber reinforced concrete are estimated by examining the attenuation and dispersion behaviors of the ultrasonic surface waves. The ultrasonic wave signals are processed with the DWT and 2D-FT to extract the attenuation coefficient and the dispersion index, respectively. In Table 2, the results of diagnosis given earlier in the plots are also summarized. In conclusion, the research findings and recommendations can be summarized as follows:

- Both diagnostic indices, namely attenuation coefficient α and dispersion index *DI*, which are calculated to quantify the overall disruption caused by the cracks in the waves, are observed to increase in a linear fashion with the crack depth.
- Among these two indices, given the regression analyses, it can be stated that the *DI* ($R^2 = 0.98$) provides improved crack-depth estimation compared to the attenuation coefficient α ($R^2 = 0.77$).
- It is found that the assessment based on the *DI* is consistent with the visual inspection for the six inspected specimens out of seven, in other words for 86% of the specimens.
- The *DI* reduces the overall variation caused by a crack in the dispersion curve into a single diagnostic feature, and hence it can be conveniently used to estimate the crack depth in structural members.

6. Recommendations for future works

Given the fact that each diagnostic index may inherit errors originated from the test configuration/setup, specimen properties, data processing techniques, etc., taking multiple diagnostic indices into account, instead of relying on only a single one, will increase the accuracy of diagnosis. Therefore, in the future, it will be beneficial to implement feature-fusion techniques to combine these two diagnostic indices discussed herein, so that a single fused index with improved reliability can be obtained.

Acknowledgments

This work was supported by The Scientific and Technological Research Council of Turkey (TUBITAK) [Reintegration Grant, Project ID: 118C022]. Authors would like to thank Amine Hatun Yumuşak and Merve Ekşiler for their contribution in generating the DIP results.

References

Acebes, M., Molero, M., Segura, I., Moragues, A. and Hernández, M.G. (2011), "Study of the influence of microstructural parameters on the ultrasonic velocity in steel-fiber-reinforced cementitious materials", *Constr. Build. Mater.*, **25**(7), 3066-3072. https://doi.org/10.1016/j.conbuildmat.2010.12.062.

ACI Committee 222R-01 (2010), Protection of metals in concrete against corrosion, American Concrete Institute, Farmington Hills, MI.

Addison, P. (2002), *The Illustrated Wavelet Transform Handbook: Introductory Theory and Applications in Science*, Institute of Physics Publishing, Bristol and Philadelphia.

Aggelis, D.G., Leonidou, E. and Matikas, T.E. (2012), "Subsurface crack determination by one-sided ultrasonic measurements", *Cement Concrete Compos*, **34**(2), 140-146. https://doi.org/10.1016/j.cemconcomp.2011.09.017.

ASTM C597-16 (2016), Standard Test Method for Pulse Velocity Through Concrete. ASTM International, West Conshohocken, PA.

ASTM C1383-15 (2015), Standard Test Method for Measuring the P-Wave Speed and the Thickness of Concrete Plates Using the Impact-Echo Method. ASTM International, West Conshohocken, PA.

Carpinteri, A., Lacidogna, G. and Niccolini, G. (2011), "Damage analysis of reinforced concrete buildings by the acoustic emission technique", *Struct. Control Health Monit.*, **18**(6), 660-673. https://doi.org/10.1002/stc.393.

Daniels, D.J. (2004), *Ground Penetrating Radar*, Institution of Engineering and Technology.

Dorafshan, S., Thomas, R.J. and Maguire, M. (2018), "Comparison of deep convolutional neural networks and edge detectors for image-based crack detection in concrete", *Constr. Build. Mater.*, **186**, 1031-1045. https://doi.org/10.1016/j.conbuildmat.2018.08.011.

du Tertre, A., Kirlangic, A.S., Cascante, G. and Tighe, S.L. (2020), "Ultrasonic inspection of asphalt pavements to assess longitudinal joints", *Road Materials and Pavement Design*. https://doi.org/10.1080/14680629.2020.1820895.

EN 14651. (2005), Test method for metallic fibre concrete – Measuring the flexural tensile strength.

Graff, K.F. (1975), *Wave Motion in Elastic Solids*, Ohio State University Press, Belfast.

Katzer, J., Kobaka, J. and Ponikiewski, T. (2020), "Influence of crimped steel fibre on properties of concrete based on an aggregate mix of waste and natural aggregates", *Materials*, **13**(8). https://doi.org/10.3390/MA13081906.

Kee, S., La, H., Basily, B. and Maher, A. (2015), "Delamination and concrete quality assessment of concrete

bridge decks using a fully autonomous RABIT platform", *Struct. Monit. Maint.*, **2**(1), 19-34. https://doi.org/10.12989/smm.2015.2.1.019.

Kirlangic, A.S., Cascante, C. and Polak, M. (2015), "Condition assessment of cementitious materials using surface waves in ultrasonic frequency range", *ASTM Int. Geotech. Test. J.*, **38**(2), 1-11.

Kirlangic, A.S., Cascante, C. and Polak, M. (2016), "Assessment of concrete beams with irregular defects using surface waves", *ACI Materials*, **113**(1), 73-81.

Kirlangic, A.S., Cascante, G. and Salsali, H. (2020), "New diagnostic index based on surface waves: Feasibility study on concrete digester tank", *J. Perform. Constr. Fac.*, **34**(6). https://doi.org/10.1061/(ASCE)CF.1943-5509.0001522.

La Malfa Ribolla, E., Rezaee Hajidehi, M., Rizzo, P., Fileccia Scimemi, G., Spada, A. and Giambanco, G. (2018), "Ultrasonic inspection for the detection of debonding in CFRP-reinforced concrete", *Struct. Infrastruct. Eng*., **14**(6). 807-816. https://doi.org/10.1080/15732479.2017.1384843.

MATLAB. (2010), version 7.10.0 (R2010a), Natick, Massachusetts: The MathWorks Inc.

Nasseri-Moghaddam A., Phillips C., Cascante G. and Hutchinson J. (2007), "Effects of underground cavities on Rayleigh waves-numerical and experimental study", *Soil Dynam. Earthq. Eng.*, **27**(4), 3000-3013.

Richart, F.E. Jr., Hall, J.R. and Woods, R.D. (1970), *Vibrations of Soil and Foundations*, Prentice-Hall, Englewood Cliffs, New Jersey.

Rodríguez-Roblero, M.J., Ayon, J.J., Cascante, G., Pandey, M.D., Alyousef, R. and Topper, T. (2019), "Application of correlation analysis techniques to surface wave testing for the evaluation of reinforced concrete structural elements", *NDT & E Int*., **102**, 68-76. https://doi.org/10.1016/j.ndteint.2018.11.003.

Song, W., Popovics, J.S., Aldrin, J.C. and Shah, S.P. (2003), "Measurement of surface wave transmission coefficient across surface-breaking cracks and notches in concrete", *J. Acoust. Soc. Am.*, **113**(2), 717-725. https://doi.org/10.1121/1.1537709.

Tallavo, F., Cascante, G. and Mahesh, P. (2009), "Experimental and numerical analysis of MASW tests for detection of buried timber trestles", *Soil Dynam. Earthq. Eng.*, **29**(1), 91-102. https://doi.org/10.1016/j.soildyn.2008.01.011.

Tang, S. and Chen, Z.Q. (2020), "Scale–Space data augmentation for deep transfer learning of crack damage from small sized datasets", *J. Nondestruct. Eval.*, **39**(3). https://doi.org/10.1007/s10921-020-00715-z.

Van Hauwaert, A., Delannay, F. and Thimus, J. (1999), "Cracking behavior of steel fiber reinforced concrete revealed by means of acoustic emission and ultrasonic wave propagation", *ACI Mater. J.*, **96**(3), 291-296.

Yang, Y., Cascante, G. and Polak, M. (2009), "Depth detection of surface-breaking cracks in concrete plates using fundamental lamb modes", *NDT & E Int.*, **42**(6), 501-512. https://doi.org/10.1016/j.ndteint.2009.02.009.

Yazici, S., Inan, G. and Tabak, V. (2007), "Effect of aspect ratio and volume fraction of steel fiber on the mechanical properties of SFRC", *Constr. Build. Mater.*, **21**(6), 1250-1253. https://doi.org/10.1016/j.conbuildmat.2006.05.025.

Zerwer, A., Polak, M. and Santamarina, J.C. (2003), "Rayleigh wave propagation for the detection of near surface discontinuities: Finite element study", *J. Nondestruct. Eval.*, **22**(2), 39-52. https://doi.org/10.1023/A:1026307909788.

JK